Pulse Testing for Monitoring the Thermal Front in Aquifer Thermal Energy Storage

Peter A. Fokker[1,2,3], Eloisa Salina Borello[1*], Dario Viberti[1], Francesca Verga[1] and Jan-Diederik van Wees[2,3]

[1] Politecnico di Torino, Turin, Italy

[2] TNO – Geological Survey of the Netherlands, Utrecht, The Netherlands

[3] Utrecht University, Utrecht, The Netherlands

ABSTRACT

Seasonal storage of heat in shallow aquifers for increasing the efficiency of geothermal energy systems requires a proper monitoring strategy. We expanded our earlier work on harmonic pulse testing (HPT) to incorporate the effect of a temperature front moving into the reservoir due to injection of hot (or cold) water. Our analytical solutions were applied to monitor the thermal front evolution in a doublet system. Thermal front position and average temperature around the injector could indeed be characterized through the application of the proposed HPT interpretation. Additional analyses were carried out adding noise to evaluate the robustness of the interpretation methodology.

1. INTRODUCTION

The development of Geothermal Energy in the Netherlands is mainly associated with heating. However, traditional geothermal doublets cannot operate at their optimal power due to climate seasonality and the daily fluctuations in weather and heat demand. The economics of geothermal heat could therefore be enhanced considerably by storage that evens out heat surplus and heat demand. One of the storage possibilities currently considered is seasonal storage of heat in shallow aquifers: ATES (Aquifer Thermal Energy Storage). It would store the surplus of energy supply in the summer and harvest it in the winter. This strategy potentially increases the overall efficiency of the system.

The efficiency of an ATES system depends on the ability to recover the stored heat. Recovery depends on the distribution of reservoir properties and on the operational design. However, the geological setting, including heterogeneities in the reservoir properties, is often

* Corresponding author. eloisa.salinaborello@polito.it; DIATI Department, Politecnico di Torino, C.so Duca degli Abruzzi 24, 10129, Turin, Italy. Tel. 0039-011-0907731

24 poorly known. Further, the resulting temperature distribution is subject to uncertainty both after injection and after production. As a result,

25 an understanding of the heat distribution is key for being able to optimize the operational efficiency. Effective monitoring of the heat

26 distribution upon injection and production of hot and cold water is thus mandatory.

27 Well testing is an important technique for the determination of reservoir properties, including flow boundaries and mobility interfaces

28 (Gringarten, 2008). Proper production/build up testing, however, requires an initial well shut-in to approximate pressure equilibrium

29 minimizing effects of pumping operations, and a well shut-in during the build-up (Bourdet 2002). Moreover, to be interpretable, the

30 registered pressure should not be influenced by activity in neighboring wells, therefore a test usually involves also a temporary interruption

31 of nearby operations. Periodic Pumping testing (Renner & Messar, 2006) also referred to as Harmonic Pulse Testing (HPT) in the reservoir

32 engineering literature (Hollaender, Hammond, & Gringarten, 2002), on the contrary, is applicable during ongoing operations and does not

33 require significant alteration of tested well net production/injection (Salina Borello et al., 2017). Furthermore, it does not require special

34 equipment: the standard well testing equipment is sufficient, provided that well-defined rate pulses are imposed and precise pressure

35 monitoring is carried out.

36 In the present contribution, we extend the pulse testing methodology to the monitoring of thermal zones around a geothermal injector well

37 or to the monitoring of a thermal energy storage system. We will apply the interpretation approach presented by Fokker et al. (2018) that

38 is based on the strong similarity existing between the derivative of the harmonic response function versus the harmonic period and the

39 pressure derivative versus time, typical for production/build-up well testing. After detailing the theoretical basis, we will demonstrate the

40 applicability of HPT to thermal front monitoring through the application of the developed analytical solution in the frequency domain to

41 the interpretation of synthetic data generated through analytical and numerical models. As a first step, we will assess the monitoring

42 feasibility of the thermal front of a geothermal doublet system. In this case, synthetic pressure data at the injector are generated analytically

43 by mimicking the presence of a cooled zone through a radial composite model. Then, we will demonstrate the feasibility of the technique

44 in monitoring the heated zone extension in an ATES scenario using a commercial numerical simulator, to overcome the hypothesis of

45 axial symmetry and a step function for the temperature change. Realistic thermal front evolution and the corresponding pressure

46 measurements at the heat storage well were generated, taking into account thermal convection and conduction and production and injection

47 histories of the two wells. Synthetic well pressure measurements were then interpreted adopting our analytical models in the frequency

48 domain, obtaining a reliable characterization of heated zone in terms of median temperature and equivalent radius.

49 **2. MATERIALS AND METHODS**

50 **2.1 Harmonic Pulse Testing**

51 The concept of Harmonic Pulse Testing was first proposed by Kuo (1972) and has been developed for the determination of hydraulic

52 parameters by several authors (Black & Kipp, 1981; Cardiff & Barrash, 2015; Despax et al., 2004; Hollaender, Hammond, & Gringarten,

53 2002), in different scenarios like two-phase flow (Fokker & Verga, 2011; Zhou & Cardiff, 2017), fractured wells (Morozov, 2013; Vinci

54 et al., 2015), fractured reservoir (Guiltinan & Becker, 2015), gas wells (Salina Borello et al., 2017), and horizontal wells (Fokker et al.,

55 2018). It was also suggested for the characterization of heterogeneous reservoirs (Ahn & Horne, 2010; Cardiff et al., 2013; Copty &

2

56   Findikakis, 2004; Fokker et al., 2012; Rosa & Horne, 1997), fault hydraulic properties (Chen & Renner, 2018), and leakage from faults

57   (Sun et al., 2015). Some real applications of HPT have been documented in the literature for heterogeneity detection in aquifers (Renner

58   & Messar, 2006; Fokker et al., 2013; Cardiff et al., 2019); single and multilayer reservoirs (Rochon et al., 2008); a gas storage field

59   confined by a lateral aquifer (Salina Borello et al., 2017), a horizontal well in a gas storage field (Fokker et al., 2018) and a geothermal

60   system (Salina Borello et al., 2019).

61   Harmonic Pulse Testing imposes the regular alternation of two rate values in a well, called Pulser. Combinations of different productions

62   and/or injections or production/injection alternated with well shut-in, are possible. The effect is a pressure response that is also periodic.

63   Then the harmonic components in both the rate and the pressure are determined through Fourier analysis, possibly preceded by pressure

64   detrending (Viberti, 2016; Viberti et al., 2018). The pressure-rate relationship depends on the physics of the reservoir response and the

65   parameters in the physical correlations. When the proper models are used, interpretation of the measured pressure response through an

66   inversion or parameter estimation technique can be applied to derive the reservoir properties.

67   A great advantage of HPT is that it requires neither the initial static conditions (well shut-in of the tested well), nor the shut-in of any

68   neighbor wells during the test. Under the assumption of linearity, the pressure and flow solution of a reservoir with many wells and

69   changing production rates can then be added to the solution of the harmonic test. A Fourier transformation will provide the signal

70   components corresponding to the imposed frequencies. Furthermore, there will be no frequency mixing; frequencies can be treated

71   independently.

72   We present the equations for a composite radial system, which is the approximate model for an ATES storage well that is surrounded by

73   a region of altered temperature. In a reservoir containing single-phase slightly compressible fluid, the flow is described by the equation:

74
$$\phi c_t \rho \frac{\partial p}{\partial t} = \nabla \cdot [\lambda \rho \nabla p] \tag{1}$$

75   Where $\lambda = k/\mu$ is the mobility; ϕ is the rock porosity, c_t is the total compressibility ($c_t = c_w + c_f$ where c_w is the compressibility of the

76   water and c_f is the compressibility of the formation), k is the rock permeability, μ is the fluid viscosity, ρ is the fluid density, p is the

77   pressure and t is the time.

78   When a piecewise homogeneous domain is assumed with approximately constant density, the equation (1) is linear and can be locally

79   solved analytically. We obtain:

80
$$\frac{\partial p}{\partial t} = \eta \nabla^2 p \tag{2}$$

81

82   where $\eta = \lambda/\phi c_t$ is the diffusivity constant. We consider each frequency component independently because they can be isolated through

83   Fourier transformation as noted above.

84   We apply a harmonic injection rate:

3

85
$$q_{well} = q_{\omega}e^{i\omega t} \tag{3}$$

86 Eq. 3 is equivalent to $q_{well} = q_{\omega}\big(\cos(\omega t) + i \sin(\omega t)\big)$. Thus, the real part of q_{well} represents a (co)-sinusoidal or harmonic test.

87 We write the pressure solution for each frequency as a complex-valued function that is the product of a space-dependent and a time-

88 dependent function:

89
$$p_{\omega}(\mathbf{r}, t) = g_{\omega}(\mathbf{r})e^{i\omega t} \tag{4}$$

90 The angular frequency is defined as $\omega = 2\pi/T$, where T is the cycle time of the imposed harmonic signal. This results in a time-

91 independent differential equation for g_{ω}:

92
$$i\omega g_{\omega}(\mathbf{r}) = \eta \nabla^2 g_{\omega}(\mathbf{r}) \tag{5}$$

93 For a reservoir with radial symmetry, the diffusivity equation can be rewritten into radial coordinates. We obtain:

94
$$i\omega g_{\omega}(r) = \eta \frac{1}{r}\frac{d}{dr}\left(r\frac{dg_{\omega}}{dr}\right) \tag{6}$$

95 The general solution to this equation is a superposition of two modified Bessel functions of order 0 (K_0 and I_0) (Abramowitz & Stegun,

96 1964). For convenience, we scale the solution by the injection rate amplitude q_{ω}, and we write the general solution as:

97
$$g_{\omega}(r) = q_{\omega}C_K K_0(\zeta r) + q_{\omega}C_I I_0(\zeta r) \tag{7}$$

98 where

99
$$\zeta = \sqrt{\frac{i\omega}{\eta}}$$

100 and C_K and C_I are free parameters to be determined by imposing boundary conditions. The Bessel functions have a complex argument

101 since the differential equation has a complex parameter. As a result, the solution is complex as well, and has an amplitude and a phase

102 when translated to the real domain. At the wellbore, pressure must be corrected to include skin effect (S) as shown in detail in Appendix

103 A.

104 We consider a composite system of two concentric zones around the wellbore with different temperatures (in the literature also referred

105 to as concentric-shell model (Cheng and Renner, 2018)). The applicability of this sharp-front approximation for the actual case with a

106 continuously changing temperature will be assessed later. Different temperatures imply different fluid viscosities and possibly different

107 compressibilities. Therefore, the mobility (λ), the diffusivity (η), and the associated multiplier (ζ) for the radial distance is different in the

108 two zones. The pressure expression is thus characterized by 4 free parameters (C_K^i and C_I^i for each zone i), whose determination requires

109 4 conditions. These are given by two boundary conditions (reservoir inflow from the wellbore corrected for wellbore storage (C); vanishing

110 pressure disturbance at infinity) and two continuity conditions at the interface between the two zones (continuity of pressure and flow

111 rate). The evaluation of the parameters for the composite radial system is provided in Appendix B. The parameters and Bessel function

4

112   evaluations depend on the reservoir and fluid parameters, the fluid front position, and the frequency. From the resulting pressure

113   expression, we can determine a response function for every harmonic component of the injection or production rate tested:

$$R_\omega^{pulser} = \frac{p_{well}}{q_{well}} = C_K^1 K_0(\zeta_1 r_w) + C_I^1 I_0(\zeta_1 r_w) + S\zeta_1 r_w [C_K^1 K_1(\zeta_1 r_w) - C_I^1 I_1(\zeta_1 r_w)] \qquad (8)$$

115   For an observer well, the expression of the response function depends on its position with respect to the thermal front (i.e. observer well

116   inside or outside the altered temperature area):

$$R_\omega^{obs} = \frac{p_{obs}}{q_{well}} = \begin{cases} C_K^1 K_0(\zeta_1 r_{obs}) + C_I^1 I_0(\zeta_1 r_{obs}) & (r_{obs} < r_1) \\ C_K^2 K_0(\zeta_2 r_{obs}) & (r_{obs} \geq r_1) \end{cases} \qquad (9)$$

118   Derivation details for eq. (8) and eq. (9) are given in Appendix B.

119   **2.2 Interpretation methodology of Harmonic Pulse Testing**

120   For the HPT interpretation, we focused on the response of the pulser well because we observed that the pulser response (R_ω^{pulser}) was

121   significantly more sensitive to variations of the heated zone than the observer response (R_ω^{obs}). Thus, eq. 8 represents the analytical

122   solution that will be employed as interpretation model. Interpretation is the process of matching test data through selection of the

123   interpretation model (radial composite, Infinite Acting Radial Flow, etc.) and characterization of model parameters. In eq. 8, C_K^1 , C_I^1 and

124   ζ_1 depend on the reservoir and fluid parameters, fluid front position and frequency. Both amplitude ($|R_\omega^{pulser}|$) and phase shift ($\angle R_\omega^{pulser}$)

125   were analyzed.

126   Data need to be preprocessed before interpretation because the model is in the frequency domain. To this end, rate and well pressure data

127   are transformed through FFT obtaining Q_ω and P_ω, respectively, which represent the signal value of each frequency component f = ω/2π.

128   The penetration depth decreases with increasing frequency (Fokker et al., 2018). Amplitude peaks, representative of the harmonic

129   components, are identified in the flow rate and pressure spectra and the response function is calculated as the amplitude ratio $R_\omega = P_\omega / Q_\omega$,

130   for each frequency component. The derivative of the amplitude ratio with respect to the logarithm of the oscillation period (R') is

131   calculated by a three point data differentiation algorithm (Bourdet, 2002). Then, the modulus of harmonic response function (|R|) and the

132   modulus of its derivative (|R'|) versus the harmonic period (T) are plotted on a log-log scale allowing an interpretation analogous to

133   conventional Pressure Transient Analysis (Bourdet et al., 1983; Gringarten et al., 1979). Flow geometries and flow regimes can be easily

134   identified on the derivative plot. In particular:

135   • |R'| showing a plateau (linear trend with slope 0 called horizontal stabilization in the Pressure Transient Analysis terminology)

136   corresponds to Infinite Acting Radial Flow. The stabilization value, i.e. the ordinate value of the trend (y_M), is proportional to

137   the investigated zone properties (Fokker et al. 2018):

$$k = \frac{B\mu}{4\pi h}\frac{1}{y_M} \qquad (10)$$

139   If the aquifer contains two zones characterized by different viscosities, two different horizontal stabilizations should be visible

140   (Figure 1). For the injector of a geothermal doublet, the undisturbed zone is the outer one. Thus, the mobility of the system can

141   be estimated from that stabilization.

5

142   • The ratio between the values corresponding to the two horizontal stabilization gives the mobility ratio (M between inner (1) and
143   outer zone (2)):

$$M = \left(\frac{k}{\mu}\right)_1 \Big/ \left(\frac{k}{\mu}\right)_2 \qquad (11)$$

145   • The critical oscillation period T* corresponds to the transition between the two zones with different mobility and can be picked
146   up from log-log plot visual inspection (Figure 1). This allows to estimate the position of the front (r_1):

$$r_1 = 1.5\sqrt{\frac{kT^*}{2\pi\mu c_t\phi}} \qquad (12)$$

148   • At high frequency, corresponding to the investigation of the near wellbore area, |R| and |R'| both show a linear trend with a unit
149   slope on the log-log plot when wellbore storage occurs (Fokker et al. 2018), i.e. when the pressure response is dominated by the
150   compression and expansion of the fluid in the well. Such phenomenon is more severe if the well volume (V) and the fluid
151   compressibility (c) are large. However, the wellbore storage can be non-negligible also in geothermal aquifers (Salina Borello
152   et al., 2019). By selecting the match point (x_M,y_M) at the intercept of the first horizontal stabilization and the linear wellbore
153   storage trend, we can quantify the wellbore storage as:

$$C = Vc_w = 2x_M\frac{kh}{\mu} = \frac{B}{2\pi}\frac{x_M}{y_M} \qquad (13)$$

155   • The distance between |R| and |R'| on log-log plot is proportional to the well damage (skin), which is responsible for an additional
156   pressure drop at the wellbore.

158   The |R| and |R'| data points vs. oscillation period are represented on a log-log plot, while phase shift ($\angle R$) vs. oscillation period is
159   represented on a semilog plot; both are compared with an analytical interpretation model obtained for a given combination of model
160   parameters values. Similarly to conventional PTA, the values of model parameters are modified, in a trial and error process, in order to
161   obtain an acceptable match of the real data. The quality of the match is typically based on visual inspection. This trial and error procedure
162   is guided by identification of the match point, the two horizontal stabilizations and the transition between them (eq. 10-13).

163   Assuming the permeability to be constant, M represents the ratio between viscosities of the outer and the inner zone. Knowing the
164   relationship between viscosity and temperature behavior, an estimate of the inner zone average temperature (T_1) is possible. The
165   methodology is still applicable in the presence of heterogeneities, provided a preliminary characterization of the permeability variations
166   inside the test investigation distance is available. Therefore, a baseline HPT should be performed before any thermal injection. A
167   comparative analysis of the test conducted during or after the injection campaign with the baseline test will allow a correct identification
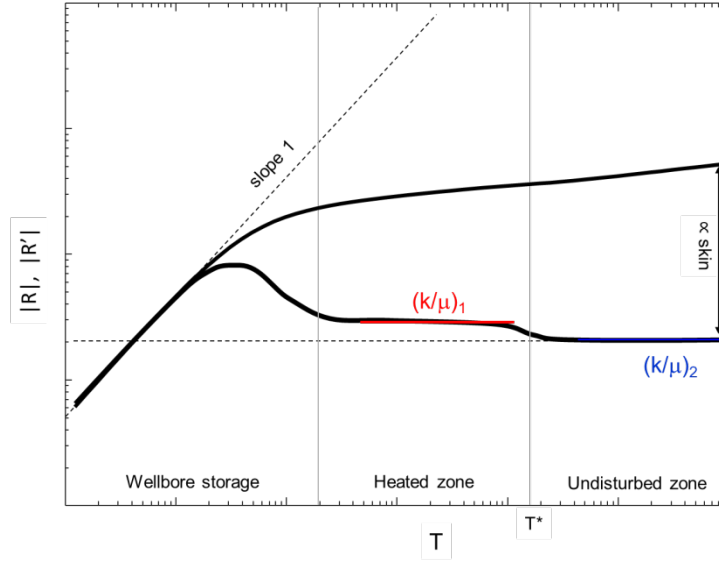168   of the temperature front.

Figure 1: **Schematic of HPT log-log plot for a radial composite model of aquifer (M=0.66)**

2.3 Design of Harmonic Pulse Testing for thermal front monitoring

The fundamental oscillation period (T_f) of HPT needs to be selected to ensure an investigation distance (r_{max}) well into the undisturbed region ($r_{max} \gg r_1$). The fundamental injection period represents the maximum oscillation period in the Fourier analysis ($T_f = T_{max}$), thus it determines the test investigation distance (Salina Borello et al., 2019):

$$r_{max} = 1.5\sqrt{\frac{kT_f}{2\pi\mu c_t\phi}} \tag{14}$$

At the other side of the spectrum, the sampling resolution determines the lowest oscillation period component detectable on the pressure signal:

$$T_{min} = 2\Delta t \tag{15}$$

Thus, the minimum distance investigated by the test, in ideal conditions (i.e. no noise) is:

$$r_{min} = 1.5\sqrt{\frac{k\Delta t}{\pi\mu c_t\phi}} \tag{16}$$

Eq. 16 may be used to calculate the sampling resolution necessary to characterize the near-wellbore heated zone. However, the harmonic components corresponding to the smaller oscillation periods can be affected by wellbore storage and skin phenomena limiting the detectability of the heated zone. The threshold oscillation period corresponding to the duration of wellbore storage effect can be evaluated by converting the time domain Chen & Bringham's criterion into the frequency domain:

7

188

$$T \leq \frac{50C\mu}{kh}e^{0.14S}$$ (17)

Chen & Bringham's criterion is widely used to estimate the duration of the effects of wellbore storage in Pressure Transient Analysis (Chaudhry, 2004).

As a consequence of eq. 17, the heated zone can be characterized if:

$$T^* \gg \frac{50C\mu}{kh}e^{0.14S}.$$ (18)

where T^* represents the critical oscillation period, i.e. the oscillation period of the harmonic component investigating the transition zone. In dimensionless terms, defining the dimensionless period through $T_D = \frac{T}{2\pi}\frac{k}{\mu c_t \phi r_w^2}$ (Salina Borello et al., 2019), we have for the transition period ($T_D{}^*$), and the maximum (T_{Dmax}) and minimum periods (T_{Dmin}):

$$T_D{}^* = \frac{1}{4.5\pi}\left(\frac{r_1}{r_w}\right)^2 \gg \frac{50C}{2\pi h c_t \phi r_w^2}e^{0.14S}$$ (19)

$$T_{Dmax} = \frac{T_f}{2\pi}\frac{k}{\mu c_t \phi r_w^2} \gg T_D{}^*$$ (20)

$$T_{Dmin} = \frac{2\Delta t}{2\pi}\frac{k}{\mu c_t \phi r_w^2} \ll T_D{}^*$$ (21)

Finally, test reliability strongly depends on the precision in the rate-change timing. In fact, errors in the rate-change timing (e_T) alter the harmonic component of frequency $f \geq 1/e_T$. Acceptable errors in timing should be properly evaluated case by case in the test design phase. In the case of thermal front monitoring the error should not mask the two horizontal stabilizations and the transition zone on the response derivative (|R'|):

$$e_T \ll T^* = \frac{\mu c_t \phi r_1^2}{2.25k}$$ (22)

The quality of the response function is less dependent on the magnitude of the two alternating rates and their precision (Salina Borello et al., 2017).

2.4 Geothermal doublet

Two cases representative of a geothermal doublet system were considered (Table 1): after one month of water injection (case 1), and after six months of water injection (case 2). For each scenario, at the end of the injection period, a periodic test was performed at the injector (Table 2). The distance from the injector well to the producing well allowed the thermal front to develop with an axially symmetric shape, not altered by production at the producing well, thus representing a perfectly radial-composite scenario. We tested the reliability of our analytical radial-composite model (eq. 8 with the constants as defined in Appendix B) against a well-established analytical radial-

8

214   composite model in the time domain (Olarewaju et al., 1989), implemented in a commercial software. A synthetic pressure response was

215   generated in the time domain and interpreted with our model in the frequency domain. Furthermore, the impact of pressure gauge noise

216   on the interpretation results was evaluated in a set of additional simulations. In the remainder of the paper we will refer to an ideal gauge

217   when the simulated pressure response is not affected by noise and to a noisy or realistic gauge when the simulated pressure response is

218   affected by gauge accuracy.

219   Synthetic data were generated by simulating the dynamic propagation of the temperature front with a single active well numerical

220   simulator for fluid dynamics in porous media accounting for thermal effects (Verga et al., 2008, Verga et al., 2011, Verga et al., 2014).

221   The resulting temperature profiles are shown in Figure 2. The thermal front distance from the injector well, calculated as the distance at

222   which the temperature reaches the average value between injection and reservoir temperature (60 °C in the considered validation cases)

223   is 22 m for case 1 and 52 m for case 2 (Figure 2).

224   In order to validate our solution against a well-established analytical solution, the pressure response to the pulse test was also simulated

225   with a commercial analytical software in the time domain, where the thermal front was mimicked with a fixed mobility ratio between the

226   two zones; the heated zone extension and the mobility ratio were defined according to the results of the numerical simulation (Figure 2);

227   a sampling rate of 1 sec was imposed (Figure 3). This gives the response of an ideal pressure profile not affected by noise that is used for

228   validation purposes.

229   Finally, Gaussian noise was added to the simulated pressure data to mimic the response of a crystal quartz gauge characterized by an

230   accuracy of ±0.083 bar (Schlumberger, 2016) (Figure 3), to verify the robustness of the interpretation methodology to noise.

231

232
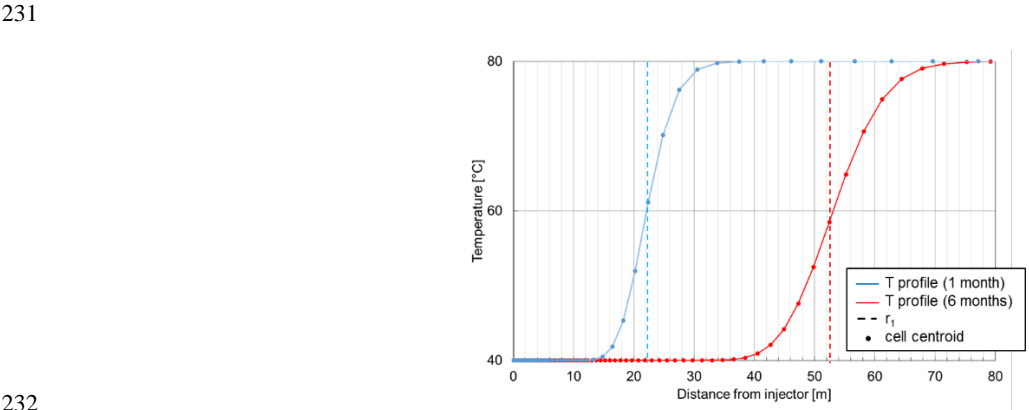
233   **Figure 2: Numerically simulated thermal profiles: 1-month injection (light blue) vs 6 months of injection (red) and corresponding**

234   **radial composite radii (dotted lines).**

235

236

9

237   **Table 1: Simulation parameters for well, rock and water for the geothermal doublet scenario**

Aquifer data	
permeability (mD)	60
porosity (-)	0.2
reservoir temperature (°C)	80
pressure (bar)	200
depth (m ssl)	2000
net pay (m)	100
Well	
radius (m)	0.1
skin (-)	2
Rock	
compressibility (bar^{-1})	2.00E-05
thermal conductivity (W/K m)	2
heat capacity (J/kg K)	850
density (kg/m^3)	2600
Water	
compressibility (bar^{-1})	4.00E-05
thermal conductivity (W/K m)	0.6
heat capacity (J/kg K)	4148
salinity (ppm)	1000
density (kg/m^3)	1001
viscosity (mPa s) @ res temperature	0.34
viscosity (mPa s) @ inj temperature	0.66
injection temperature (°C)	40

238   **Table 2: Rate history of geothermal doublet scenarios**

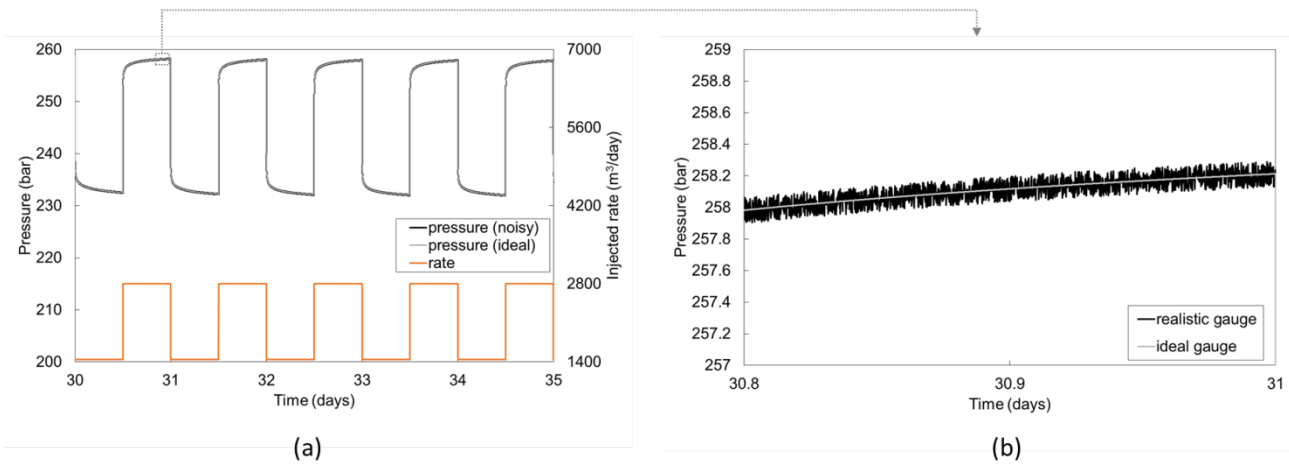| Scenario	Test	Duration/period (days)	Rate (m³/min)	Rate variation (m³/min)	number of periods (-)
case 1	injection operations	30	2	-	-
	HPT1	1	1.5	± 0.5	5
case 2	injection operations	180	2	-	-
	HPT2	1	1.5	± 0.5	5

239

240

10

(a)

(b)

Figure 3: Case 1: ideal pressure gauge (gray), generated with the analytical radial-composite model in the time domain (Olarewaju et al., 1989) and noisy pressure gauge (black) generated by adding Gaussian noise to the ideal gauge; (a) full 5-period duration, and (b) zoom.

2.5. Numerical model of ATES

Heat storage cycles were simulated through a commercial 3D fluid-dynamic reservoir modeling tool taking into account the thermal phenomena. The synthetic aquifer model was based on a real formation, a possible candidate for ATES application in the Netherlands. Well, rock and water properties are reported in Table 3; annual heat storage cycle rate histories are reported in Table 4. The aquifer is characterized by 7 layers (numbered, in the following, from 1 to 7 starting from the top) of permeability ranging from 120 mD to 53797 mD. A sketch is provided in Figure 4. Two layers are open to production/injection: number 3 and 5 from the top. They are characterized by permeability k_h=10760 mD and k_z = 2690 mD and porosity ϕ = 0.37, separated by inter-layer 4 with porosity ϕ = 0.5 and permeability k_h = 2391 mD and k_z = 24 mD. Layer 2, at the top of the upper perforated layer has similar properties (ϕ = 0.55, k_h = 2391 mD, k_z = 24). Simulations of the whole domain with a grid refinement 10 m x 10 m x 10 m in the well area (Figure 5) show that the upper perforated layer behaves as separated in terms of pressure response, due to the high permeability contrast. The temperature exchange between the upper perforated layer and the surrounding layers is also negligible compared to the exchange within the layer. For these reasons, a radial composite model should fit the interpretation of tests performed on such layer. We therefore focused on the upper layer only and simulated it as a single numerical layer of 1128 m x 1128 m areal extension and 30 m thickness. A significant grid refinement (cells of 4m x 4m) was imposed in an area of about 900 m x 900 m containing the wells, with the double aim of correctly simulating the pressure gauge response and accurately describing the thermal front. Further away the grid size was increased to 20 m x 20 m and finally to 200 m x 200 m. The simulation grid is shown in Figure 6. The gauge was supposed to be in the upper perforated layer, at 330 mssl. The initial pressure at datum was assumed hydrostatic (i.e., 33 bar); the initial temperature of the layer was 20 °C.

11

263   **Table 3: Simulation parameters for well, rock and water.**

Well	
radius (m)	0.7874
skin (-)	0
Rock	
compressibility (bar^{-1})	2.18E-05
thermal conductivity (W/K m)	2.4
heat capacity (J/kg K)	850
density (kg/m^3)	2100
reservoir temperature (°C)	20
Water	
compressibility (bar^{-1})	4.00E-05
thermal conductivity (W/K m)	0.6
heat capacity (J/kg K)	4148
salinity (ppm)	20000
density (kg/m^3)	1016
viscosity (mPa s) @ res. temp.	1.13
viscosity (mPa s) @ inj. temp.	0.338
injection temperature (°C)	90

264

265

266

267   **Table 4: Annual heat storage cycle.**

	duration (days)	Rate Well0 (m^3/day)	Rate Well1 (m^3/day)
summer	90	-3888	3888
autumn	60	0	0
winter	150	2328	-2328
spring	60	0	0

268

269

k_h = 53797 mD, k_z = 13449 mD
k_h = 2391 mD, k_z = 24 mD
k_h = 10760 mD , k_z = 2690 mD
k_h = 2391 mD, k_z = 24 mD
k_h = 10760 mD , k_z = 2690 mD
k_h = 8369 mD, k_z = 2092 mD
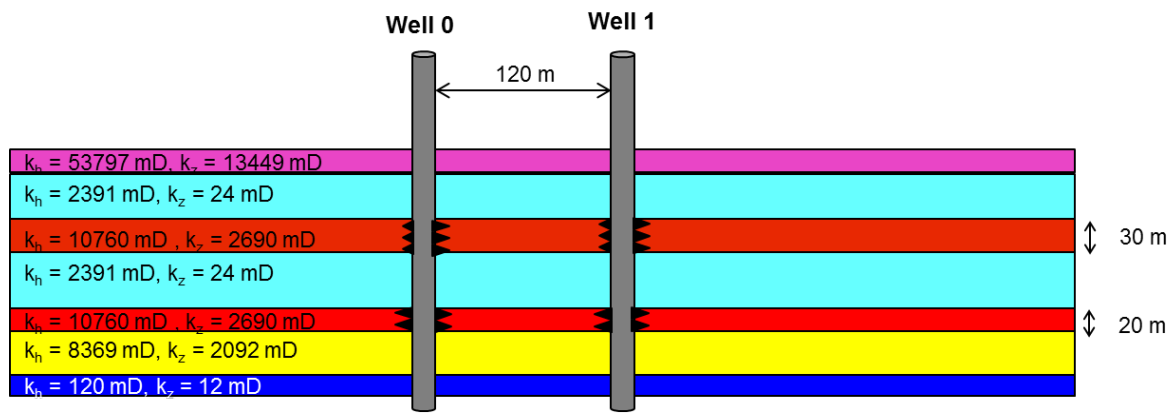k_h = 120 mD, k_z = 12 mD

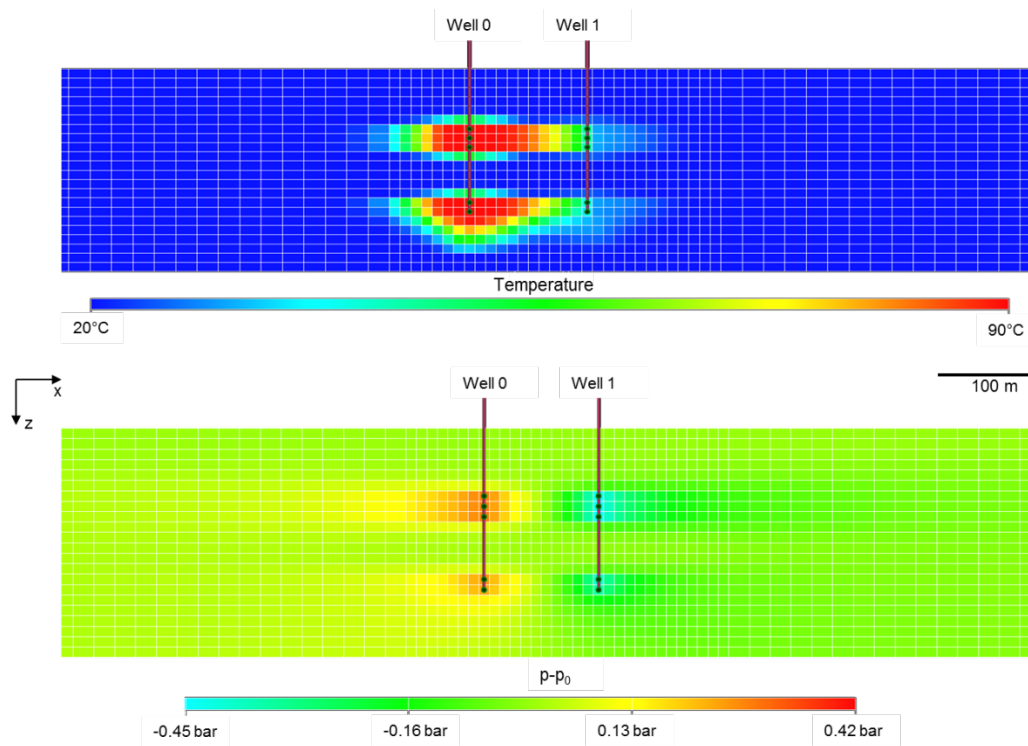270   **Figure 4: Sketch of aquifer layers (x-z cross section)**

271

272   **Figure 5: Preliminary simulation results after the 5th summer of injection (zoom of x-z cross section). Grid refinement 10m x10m**
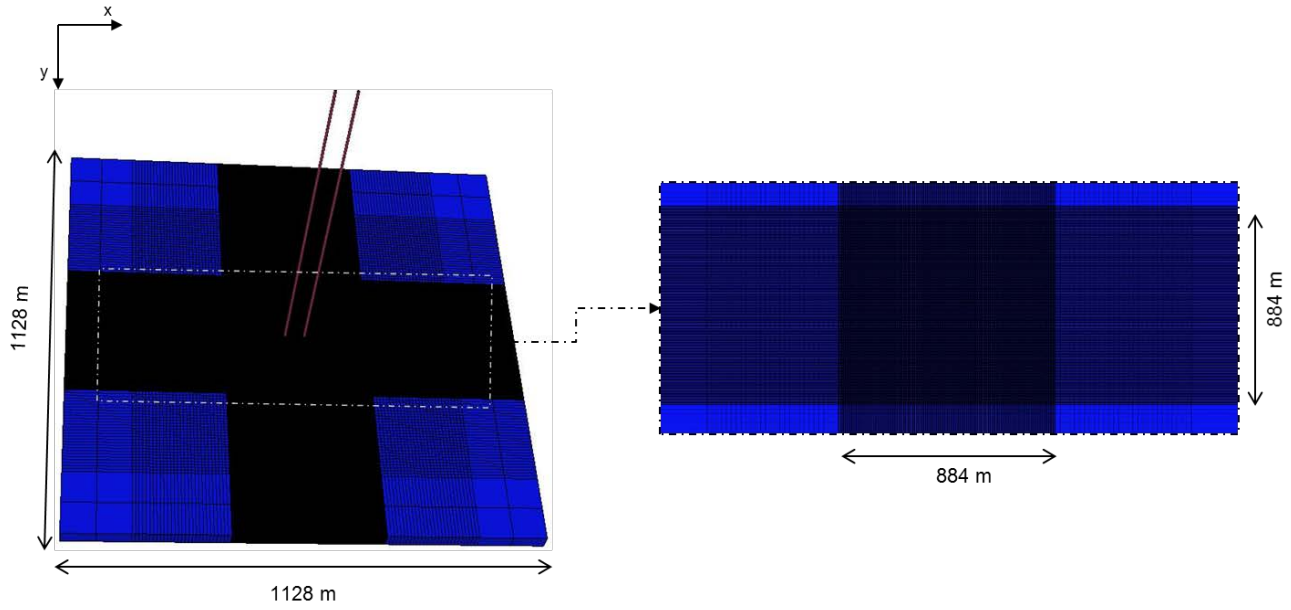
273   **x10m.**

274

13

275

Figure 6: Grid for final simulations (top view and zoom).

The same commercial software was used to simulate the HPTs pressure response, to verify the capability of the test in monitoring the heat front. The thermal front was monitored after the 5th summer of storage (4 complete storage cycles), after the subsequent winter, and again after the 15th summer of storage (14 complete storage cycles). Each test was conducted after a shut in period of one day. The data for the three HPTs in terms of test starting time, fundamental oscillation period (T_f), oscillating rates and number of oscillation periods are summarized in Table 5. Pressure and rate data are shown in Figure 7. The HPT fundamental oscillation period (T_f) was set to 6 h (3h of injection and 3h of shut-in) to assure an investigation distance far enough to explore the undisturbed region (see eq. 14). Sampling resolution was set to $\Delta t = 1$ s to be able to characterize the heated zone properties (see eq. 16). Thus, in ideal conditions (i.e. no noise) with the applied setting we can explore the circular area between $r_{min} = 25$ m and $r_{max} = 2580$ m from Well1. In dimensionless terms (eq. 20-21), we have $70 < T_D < 7.6e5$. Preliminary synthetic tests confirmed that the first horizontal stabilization was hardly detectable with $\Delta t > 1$s.

Table 5: HPT tests for heat front monitoring on Well 0.

HPT Test	HPT starting time	T_f (h)	Rate 1 (m3/day)	Rate 2 (m3/day)	Number of periods (-)
HPT1	after 5th summer	6	1396.8	0	5
HPT2	after 5th winter	6	1396.8	0	5
HPT3	after 15th summer	6	1396.8	0	5

14

288

289
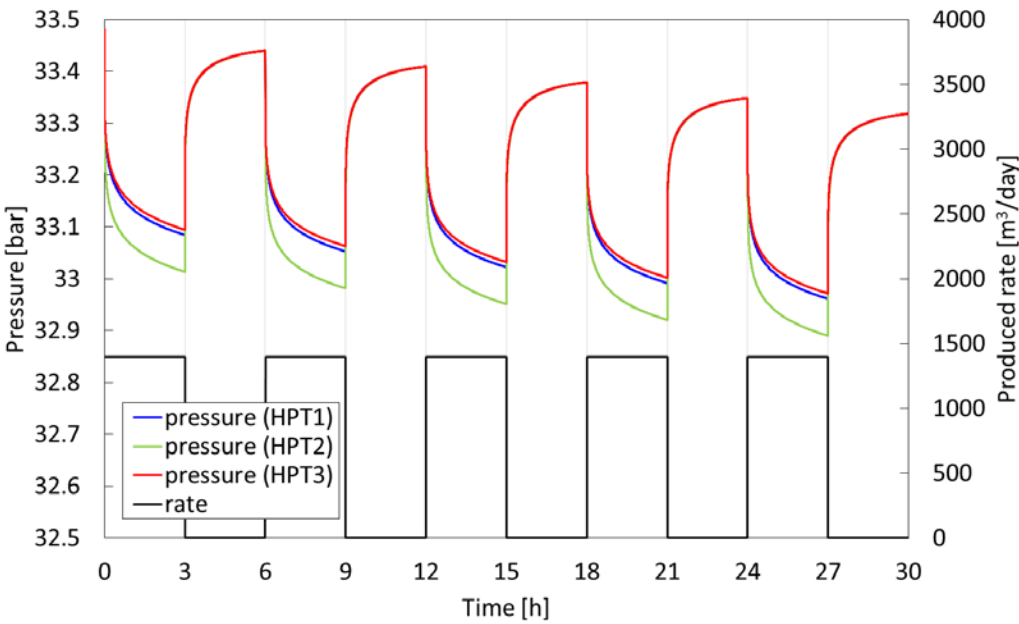
Figure 7: Simulated pressure data (red, blue, and green curve, left axis) from harmonic pumping tests 1 to 3 (see Table 5) at tested well (Well0) with the flow-rate protocol given by the black curve (right axis)).

292

3. RESULTS

3.1 TEST ON GEOTHERMAL DOUBLET

Our model was initially validated against a conventional analytical radial composite model adopted for the Geothermal doublet, assuming step-change temperature profiles. For the ideal gauge, the dimensionless log-log plot in the frequency domain (representing $|R_D|$ and $|R_D'|$ as defined in paragraph 2.2) and the analytical interpretation model are shown in Figure 8a. Case 1 is depicted in blue, while case 2 is depicted in red. In both cases, the model provides a good match of the data and a correct value of the inner thermal zone radius. Analysis of the phase shift ($\angle R$) confirms the interpretation (Figure 9a). The same behavior (Figure 10) is observed when considering pressure data generated with the numerically simulated temperature profiles (Figure 2): except for the very beginning of the transition zone, the amplitude and phase behavior is very similar to the one of the step-change profile assumption. The noisy-gauge analysis is shown in Figure 8b and Figure 9b. In both cases the inner radius is still detectable. In fact, the noise mostly affects the first stabilization, while the transition zone and the second stabilization can be clearly detected (Figure 8b); a similar influence is observed on phase shift (Figure 9b). Therefore, HPT interpretation provides a reliable monitoring of the thermal front evolution.

The complete injection history is known in these synthetic cases and the pressures are not affected by interference phenomena. Therefore,

15

306   conventional Pressure Transient Analysis (PTA) in time domain (Bourdet et al, 1984) can also be applied. The corresponding log-log plot

307   for a single injection period is shown for both the ideal gauge (Figure 11a) and the noisy gauge (Figure 11b) in dimensionless terms

308   (Bourdet, 2002). Based on that, results obtained in time and frequency domains can be directly compared (Figure 8a vs Figure 11a for the

309   ideal gauge; Figure 8b and Figure 11b for the noisy gauge) and superposed on the same log-log plot (Salina Borello et al. 2019).

310   Comparison of Figure 8b and Figure 11b shows the different impact of noise in time domain (PTA) and frequency domain (HPT).

311   Conventional PTA is mainly affected by noise in the part of the curve, corresponding to the formation volume containing the thermal

312   front (middle-time in PTA terminology). HPT is affected by noise in the part of the curve, representing the high-frequency components

313   (smaller T) which investigate the near wellbore area (early-time in PTA terminology). As a consequence, the thermal front evolution can

314   be more easily detected through HPT interpretation in the frequency domain. Furthermore, a combined analysis, obtained superposing

315   PTA and HPT curves in dimensionless terms, can improve interpretation reliability minimizing uncertainties. The combined analysis

316   follows three steps: (1) superposed representation of PTA and HPT curves in dimensionless terms (Figure 12a); (2) application of a low-

317   pass filter to both time data and frequency data to obtain a single clean derivative plot (Figure 12b); (3) interpretation of the obtained

318   derivative plot with the presented frequency model.

319

320

321

322

323   **Figure 8: Comparison of reservoir response after 1 month of injection (blue) vs. after 6 months of injection (red): frequency**

324   **analysis of the ideal gauge (a) and of the noisy gauge (b), reported in amplitude of dimensionless response ($|R_D|$) and amplitude of**

325   **dimensionless response derivative ($|R_D'|$) vs. dimensionless oscillation period (T_D); data generated with the analytical radial-**

326   **composite model in the time domain (Olarewaju et al., 1989).**
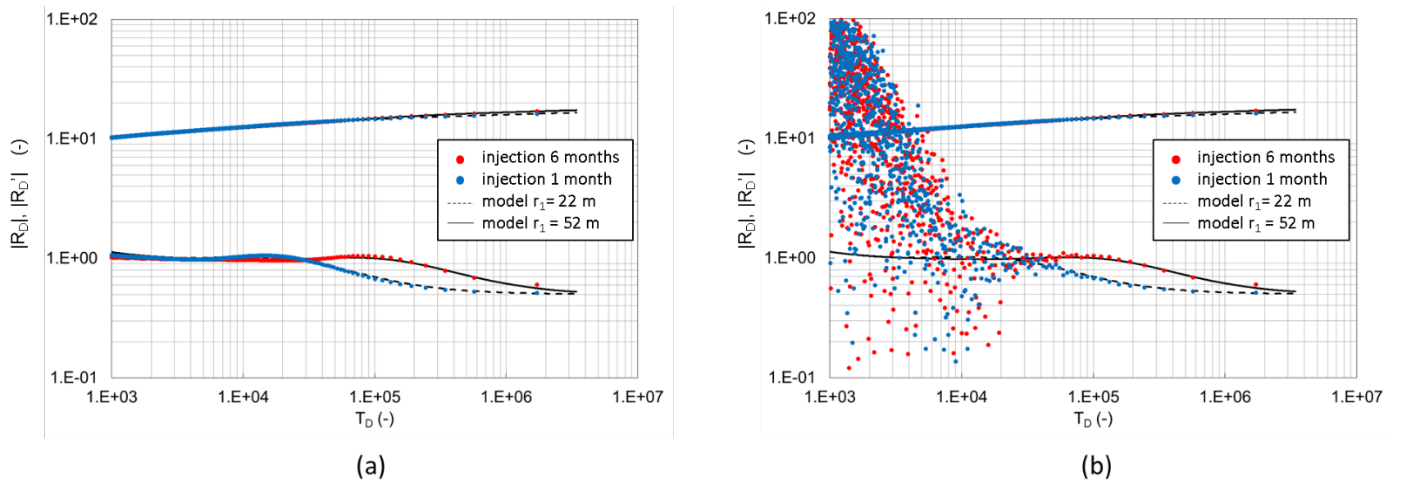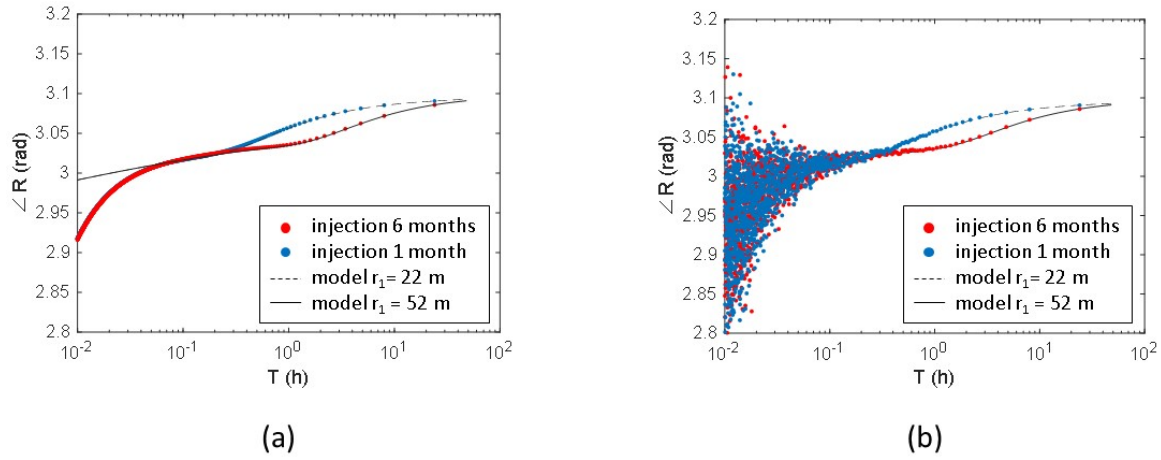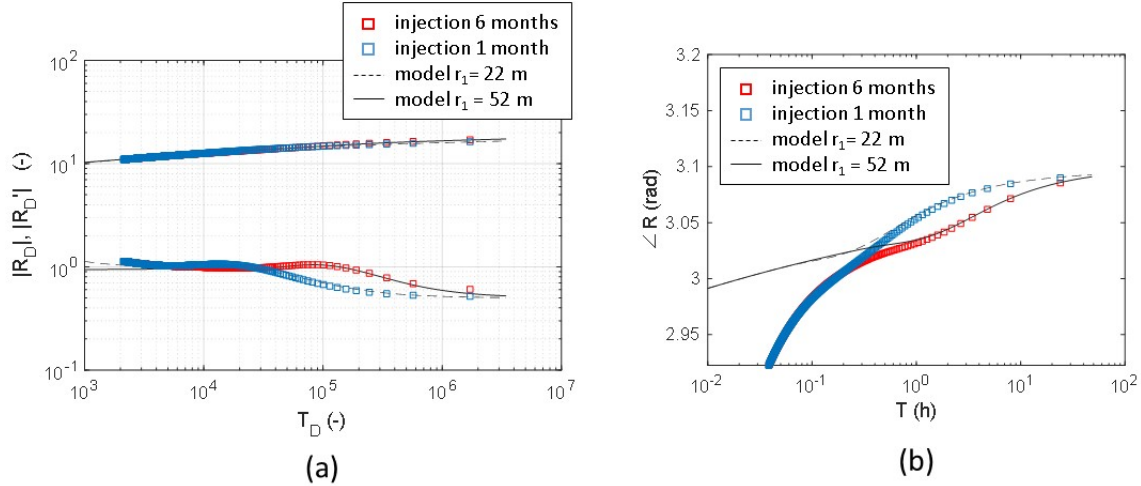
16

327

328

(a)

(b)

329

Figure 9: Comparison of reservoir response after 1 month of injection (blue) vs. after 6 months of injection (red): frequency analysis of the ideal gauge (a) and of the noisy gauge (b), in terms of phase shift (∠R) vs. oscillation period (T); data generated with the analytical radial-composite model in the time domain (Olarewaju et al., 1989).
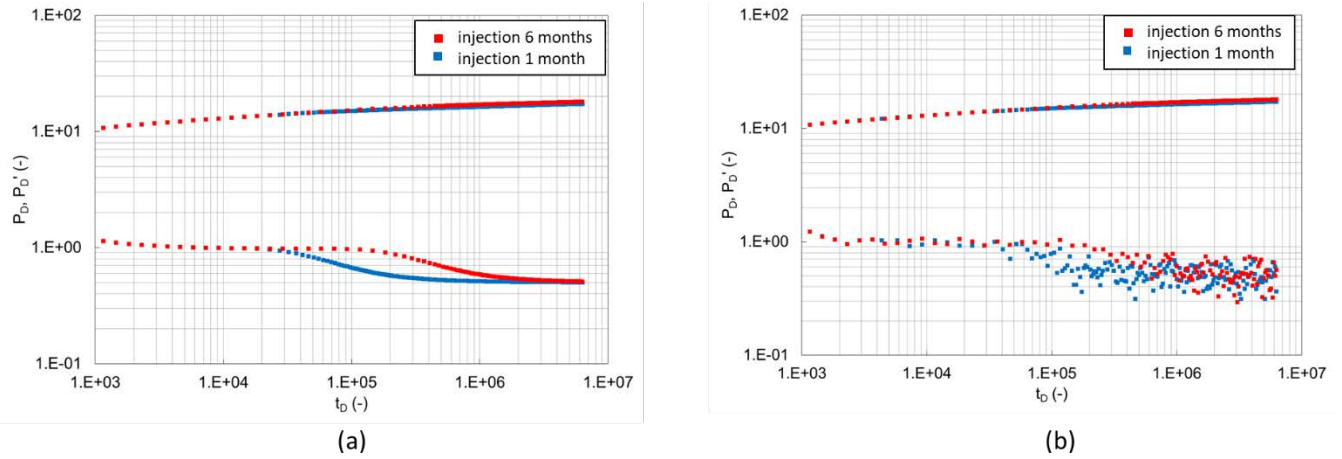
333

(a)

(b)

334

Figure 10: Comparison of the reservoir response in the active well (pulser) after 1 month of injection (blue) vs. after 6 months of injection (red): frequency analysis of the response amplitude (|R|) and amplitude derivative (|R'|) (a) and phase shift (∠R) (b); data generated with the numerical simulator accounting for thermal effects.

17

338

(a)   (b)

339

Figure 11: Comparison of reservoir response after 1 month of injection (blue) vs. after 6 months of injection (red): conventional Pressure Transient Analysis of the ideal gauge (a) vs. the noisy gauge (b), reported in dimensionless pressure (P_D) and dimensionless pressure derivative (P_D') vs. dimensionless time (t_D); data generated with the analytical radial-composite model in the time domain (Olarewaju et al., 1989).


(a)   (b)

346
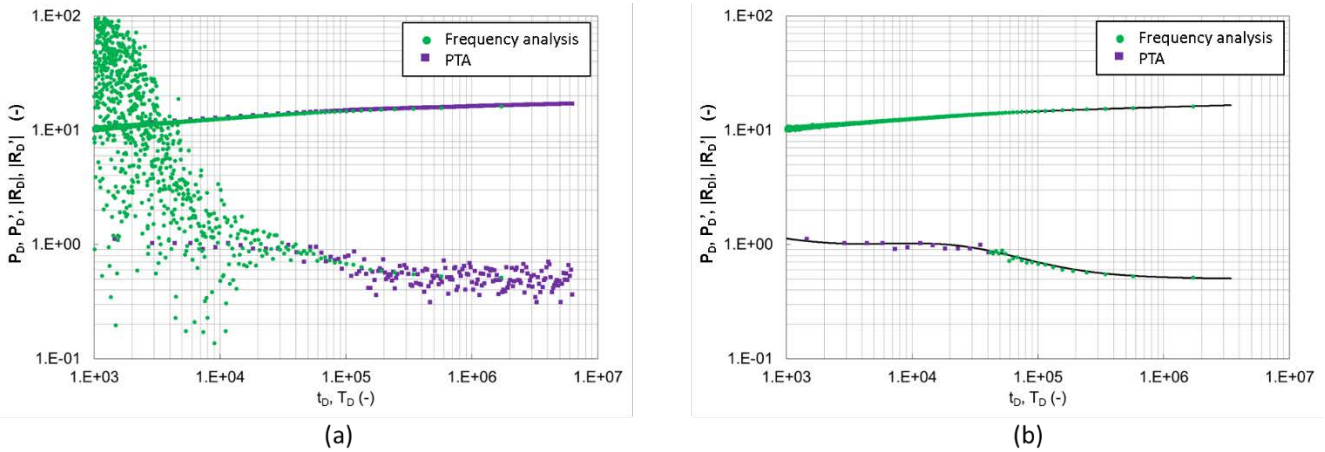
Figure 12: Maximization of information extraction from the noisy gauge by combining the analysis of time and frequency data in dimensionless terms (case1): (a) superposition of time and frequency analysis in dimensionless term; (b) application of low-pass filter to both time data and frequency data to obtain a single clean derivative plot; data generated with the analytical radial-composite model in the time domain (Olarewaju et al., 1989).

18

351

3.2 APPLICATION TO ATES

352 **3.2 APPLICATION TO ATES**

353 In the after-summer scenario of the 5th storage cycle (Figure 13a), the simulated temperature changes gradually, but not linearly, from the

354 injection temperature (90°C) to the temperature value in the proximity of the front (about 60°C), beyond which an abrupt change towards

355 the initial aquifer temperature (20°C) is observed. Due to the simultaneous production in Well1, the heated zone is off-centered with

356 respect to Well 0; it elongates toward producing Well 1, thus assuming an almost oval shape. Temperature distribution on the cross section

357 along the line connecting the two wells is provided in Figure 14 .

358 After seven months, in the after winter scenario (Figure 13b), the situation is significantly different. The temperature around Well 0 has

359 decreased to 50-70°C (Figure 14) and the heated zone extension has decreased, too. Pushed by the cold-water injection at Well 1, the

360 thermal front position along the intra-well direction moves towards Well 0 and the shape of heated zone becomes irregular. With the

361 progression of seasonal cycles, the after-summer heated zones tend to expand, becoming rounder (Figure 13c).

(a)

(b)

100 m

(c)

362

19
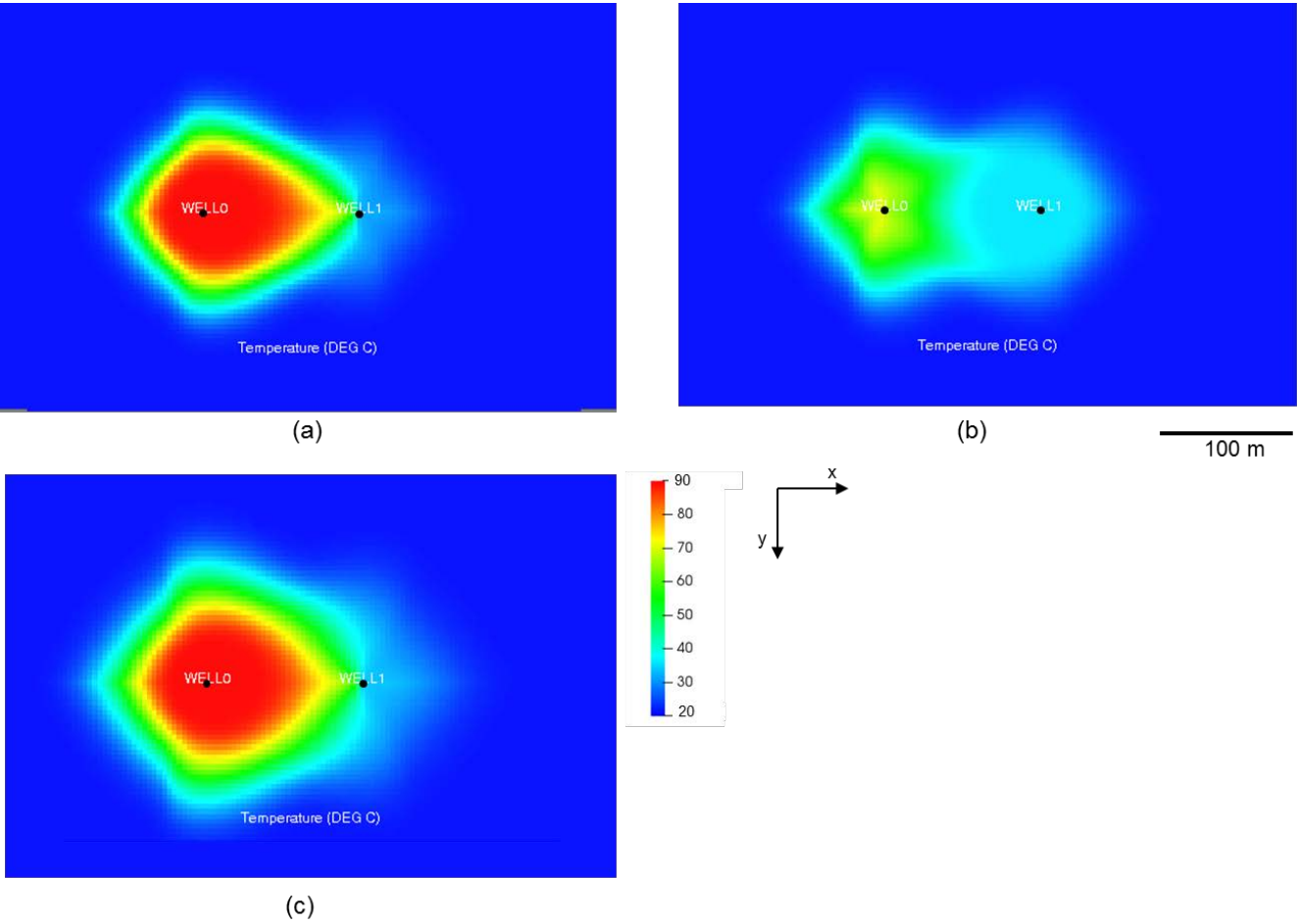
363 **Figure 13: Simulation results: comparison between temperature profiles (a) after summer of the 5th storage cycle, (b) after winter**

364 **of the 5th storage cycle and (c) after summer of the 15th storage cycle; zoom of top views.**

365
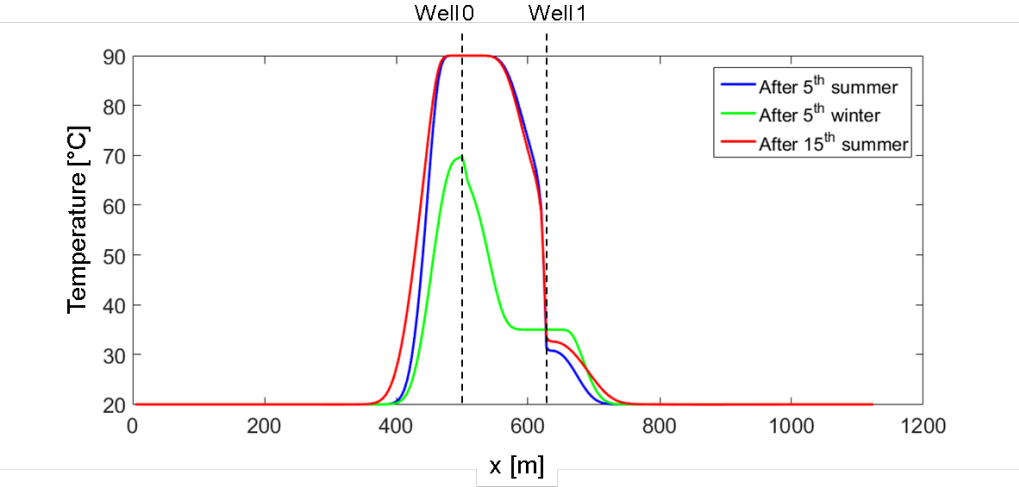
366

367 **Figure 14: Temperature distributions along the x-directrix crossing the two wells.**

368 The pressure trends of the simulated HPTs were analyzed in the frequency domain as described in section 2.2. Log-log plots of the moduli

369 of R and R' versus oscillation period ($2\pi/\omega$) and semilog plots of the phase of R versus oscillation period are shown in Figure 15. Data

370 were interpreted with our radial composite model in the frequency domain (eq. 8) to give an estimate of the extension of inner zone radius

371 (r_1) and of the mobility ratio between inner and outer zone (M), leading to an estimate of the inner zone average temperature (T_1) (Table
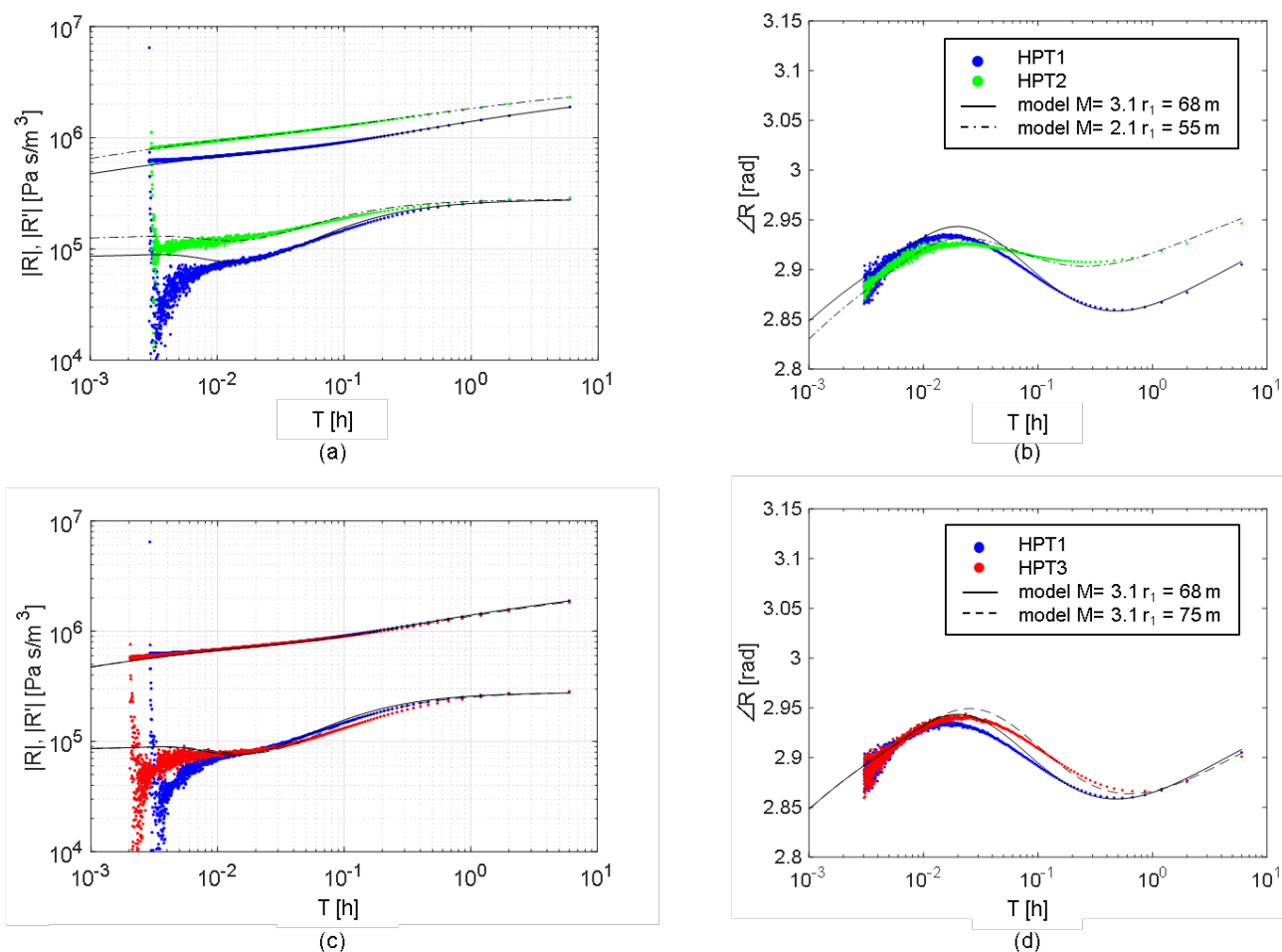
372 6).

20

373

Figure 15: HPT results: comparison between reservoir response after summer (blue) vs. after winter (green) of the 5th storage cycle in terms of (a) amplitude (|R|) and amplitude derivative (|R'|) and (b) phase shift (∠R); comparison between reservoir response after summer of the 5th storage cycle (blue) vs. 15th storage cycle (red) in terms of (c) amplitude and amplitude derivative and (d) phase shift.

For all tests (Figure 15), the second stabilization allowed for correct identification of a permeability value of about 11D and a zero skin value. Comparing after-summer and after-winter derivatives (Figure 15a), a significantly different first stabilization is observable, which corresponds to a different near-wellbore viscosity and therefore a different temperature. The extent of the near-wellbore heated zone indicated by the after-summer derivative is also significantly larger than the extent indicated by the after-winter derivative. When comparing the derivatives of tests conducted after-summer of the 5th and of the 15th storage cycle (Figure 15c), the level of the first stabilization is practically the same, indicating similar temperature, but a difference is observed for the extent of the heated zone. The size is slightly larger after the summer of the 15th cycle. Phase shift analysis (Figure 15b and Figure 15c) confirms the interpretation from the modulus of the derivative of the response and allows a better calibration of the heated zone extension, showing a good sensitivity even to

21

386 small heat zone changes, as in HPT1 vs HPT3 (Δr_1 =10%). This is in accordance with Cheng & Renner (2018), who documented that

387 phase shift is a particularly sensitive tool for concentric-shell models.

388 **Table 6: Tests interpretation results with radial composite model in the frequency domain compared with the approximation of**

389 **the simulated heated zone to an equivalent circumference centered in Well 0.**

HPT Starting time	Radial composite HPT interpretation			Numerical simulation		
	$M = \mu_2/\mu_1$	T_1 (°C)	r_1 (m)	heated zone (°C)	T_m (°C)	r_{eq} (m)
after 5th summer	3.1	84	68	55°-90°C	83.4°C	69.8
after 5th winter	2.1	58	55	45°-70°C	55.9 C°	50.9
after 15th summer	3.1	84	75	55°-90°C	80°C	78.9

390

391 We already indicated that the simultaneous injection and production in the two wells causes a distortion from axial symmetry. The heated

392 zone is neither centered around Well 0, nor circular (Figure 13). To facilitate a quantitative comparison between the numerical solution

393 and the radial composite model, we calculated an equivalent radius of the heated zone from the temperature map. First, we calculate a

394 threshold temperature ($T_{threshold}$) as the average between the temperature at the wellbore and far into the reservoir, yielding $T_{threshold} =$

395 $55 \, °C$ in the after-summer scenario and $T_{threshold} = 45 \, °C$ in the after-winter scenario. Then we applied $T_{threshold}$ as a temperature filter

396 to identify the heated zone and we calculated the median temperature values (T_m) of the selected cells. We approximated the heated zone

397 with an equivalent circumference, i.e. the circumference with radius $r_{eq} = \sqrt{\frac{A}{\pi}}$, that have an area equivalent to the heated zone (see Figure

398 16). The obtained approximation of the heated zone are also reported in Table 6. A good agreement was observed in all scenarios both in

399 terms of median temperature (T_m), which differs from the estimated temperature (T_1) by less than $4°C$, and in terms of heated equivalent

400 radius (r_{eq}), which differs from the interpreted r_1 less than 10%. We conclude that the approximation with a circular heated zone and a step

401 function for the temperature fits the synthetic data, and that the numbers derived for heated area and temperature change close to the

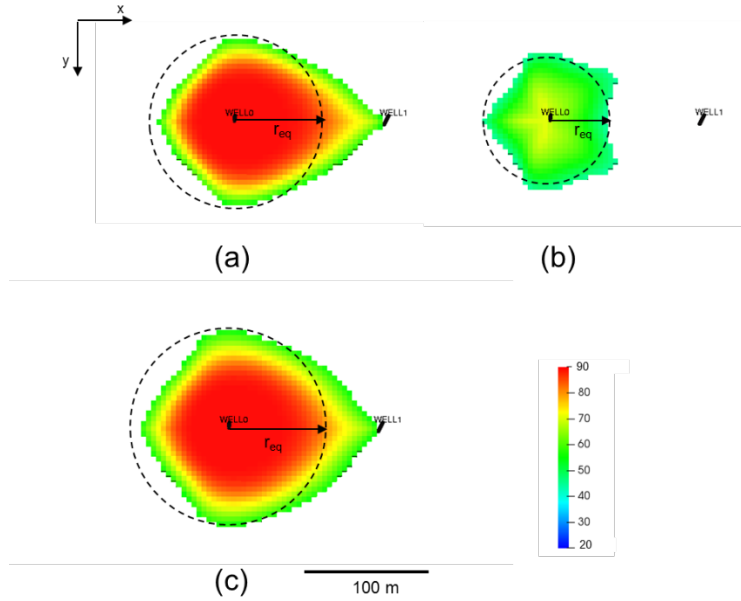402 injector characterize the actual system well.

22

Figure 16: Approximation of the heated zone with the equivalent circumference centered in Well 0 (a) after 5th summer, (b) after 5th winter and (c) after 15th summer.

4. DISCUSSION

To correctly design and perform an HPT test for heat-zone monitoring in an ATES system, some issues must be considered. To assure test interpretability, the first and the second horizontal stabilizations, representative of the heated zone and the undisturbed zone, respectively, must be clearly detectable on the log-log plot of the response derivative (see section 2.2). Thus, a proper test design is necessary (section 2.3). In the first place, such a design includes a duration of the fundamental oscillation period (i.e. the sum of the durations of the two alternating constant rates) that is long enough to investigate the undisturbed zone (eq. 14). In the presented ATES case, in which the permeability is extremely high (about 11 D), an oscillation period $T_f \geq$ 6h is sufficient to capture the stabilization corresponding to undisturbed conditions (Figure 15). Considering that 5 oscillations are required (Salina Borello et al., 2017), the total test duration is 30 h, which is compatible with the storage operations. On the one hand, high permeability allows reducing test duration; on the other hand, it implies the need of high precision in the test execution (eq. 22) and a high pressure sampling rate (eq. 16). In fact, the first stabilization, representative of the heated zone, is investigated by high frequency components. As an example, in the presented ATES case, the first horizontal stabilization covers oscillation periods in the range 0.003- 0.03h (from 10 s to less than 2 min). At the same time, these fast oscillation responses are impacted most by the wellbore storage. Thus, to be able to capture the first stabilization, the HPT test data must have: 1) a pressure sampling rate significantly below this range (i.e. $\Delta t << 10$ s); 2) rate changes performed fast enough in order to also be within this range (i.e. $e_T \leq 10$ s). Still, the wellbore storage effect may pose a lower limit to the observable radii of thermal fronts. In case of high-permeability formations, as in the considered ATES example, gauge accuracy can have a significant impact on detectability of the first stabilization. However, a combined analysis in both frequency and time domain, when feasible, can

23

423   significantly enhance interpretation reliability.

424   Data interpretability of a noisy response spectrum could also be improved by the joint interpretation of a sequence of two or more HPTs

425   characterized by different fundamental oscillation periods and therefore focusing on different investigated areas. In fact, as already

426   discussed by the authors (Salina Borello et al., 2019), the area investigated by the test is directly proportional to the square root of the

427   fundamental oscillation period T_f (eq. 14). Moreover, the harmonic components are odd fractions of fundamental oscillation period (T_f,

428    $T_f/3$, $T_f/5$, $T_f/7$, …). As a consequence, in the frequency analysis the density of points in a range of T values corresponding to a horizontal

429   stabilization depends on T_f. Moreover, along with noise on recorded pressure due to gauge accuracy, imprecision on rate changes (delay

430   and/ or advance) is responsible of noise on the response spectrum as well. Our experience on real cases (Salina Borello et al. 2017, Salina

431   Borello et al. 2019) shows that irregularities on rate changes are often higher for tests characterized by a longer T_f, which implies that

432   usually only the first 10-20 harmonic component (T_f, $T_f/3$, $T_f/5$, etc) are undisturbed. Analogously to eq. 14, the lower limit of the

433   investigation area covered by N interpretable components is directly proportional to the square root of $T_f/(2N-1)$. Thus, two subsequent

434   HPTs can be designed to better focus the investigations separately on the inner zone and on the outer zone.

435   When the test is well designed, changes of the heated zone within the storage cycle (i.e. between after-summer and after-winter) as well

436   as gradual changes over the years are detectable on the log-log plot from the variations in value and position of the first horizontal

437   stabilization observable on the response derivative (Figure 15). Clearly, the higher the viscosity contrast, the easier the detection on the

438   log-log plot, due to the larger difference between the horizontal stabilization levels for the two zones. However, relatively small values of

439   the viscosity contrast already allow the application of our methodology. Only values near to M=1, such as.0.75 <M<1.25, could be critical.

440   Similar criticalities arise if the heated zone extension is very limited. Harmonic Pulse Testing is thus suitable for heated-zone monitoring

441   in a wide range of viscosity contrasts.

442   The radially symmetric model in the test interpretation may not exactly correspond to reality, where the shape of the heated zone may be

443   non-symmetric because of the second well in the ATES doublet system (Well 1, in Figure 13) or because of other heterogeneities. As a

444   consequence, the prediction of the thermal front position between the two wells is subject to uncertainty. In addition, the actual heat front

445   is gradual rather than a step function, therefore part of the injected heat is advancing the modeled front. However, the test interpretation

446   gives valuable information about changes in average heated zone extension and temperature (Table 6).

447   **5. CONCLUSIONS**

448   In this paper, we have expanded our earlier work on Harmonic Pulse Testing (HPT) to incorporate the effect of a temperature front moving

449   into the reservoir due to injection of hot (or cold) water. The goal was to be able to employ HPT for monitoring the heat front with

450   particular focus to Aquifer Thermal Energy Storage (ATES). Reliable monitoring requires a baseline HPT test, before injection, to assess

451   the possible presence of heterogeneities. Tests after the summer injection campaign and after the winter production campaign can then be

452   employed over the years.

453   The HPT interpretation with the presented radial composite model solution was preliminarily applied to monitor the thermal front

24

454 evolution in a synthetic doublet system showing axial symmetry and thus validated against an analytical model. The methodology provided

455 reliable estimates of thermal zone extension and average temperature around the injector for an ideal pressure gauge, not affected by noise,

456 and a realistic gauge, affected by noise.

457 Furthermore, we demonstrated that HPT can be applied to monitor the thermal front of a synthetic Aquifer Thermal Energy Storage

458 (ATES) if a proper test design is applied:

459 • duration of the fundamental oscillation period is long enough to investigate the undisturbed zone

460 • rate changes are sufficiently precise, i.e. maximum acceptable advance/delays are significantly lower than the oscillation period

461 corresponding to the thermal front expected position

462 • gauge pressure sampling is close enough to investigate the heated zone

463 Agreement was observed in all scenarios both in terms of median temperature (T_m), which differed from the estimated temperature (T_1)

464 less than 4°C, and in terms of heated equivalent radius (r_{eq}), which differed from the interpreted r_1 less than 10%.

465 The information obtained from the HPT interpretation does not exactly reproduce the shape of the heated zone of the ATES doublet

466 system, which is not a step function in temperature and is not exactly axially symmetric around the tested well. The latter is due to the

467 contemporary injection/production in the second well or to other heterogeneities in the reservoir. As a consequence, HPT interpretation

468 with the radial composite model may not correctly predict the front position in between the two wells. However, the test interpretation

469 gives valuable information on the extent of the heated zone and its temperature. Moreover, a planning of systematic HPT allows for

470 monitoring variations of the heated zone during the storage cycle and over the years, thus enabling adjustment and fine tuning of the field

471 operations.

472

473 **DATA AVAILABILITY**

474 Datasets related to this article can be found at http://dx.doi.org/10.17632/ddzcwy53vr.1, an open-source online data repository hosted at

475 Mendeley Data (Chen and Maloof, 2017).

25

476 **REFERENCES**

477 Abramowitz, M. and Stegun, I. (1964) Handbook of Mathematical Functions. Chap. 9. *Dover Publications*, New York.

478 Ahn, S., & Horne, R.N. (2010). Estimating permeability distributions from pressure pulse testing. In Proceedings ‑ S*PE Annual*
479 *Technical Conference and Exhibition*, 3:2388‑2403. Florence. https://doi.org/10.2118/134391 ‑ MS.

480 Black, J. H., & Kipp, K. L. J. (1981). Determination of hydrogeological parameters using sinusoidal pressure tests: A theoretical appraisal.
481 *Water Resources Research*, 17(3), 686‑692. https://doi.org/10.1029/WR017i003p00686.

482 Bourdet, D. (2002). Well west analysis: The Use of Advanced Interpretation Models: Handbook of Petroleum Exploration and Production,
483 3. Amsterdam: Elsevier Science B.V. ISBN: 978 ‑ 0 ‑ 444 ‑ 54988 ‑ 4.

484 Bourdet, D., Whittle, T. M., Douglas, A. A., & Pirard, Y. M. (1983). New set of type curves simplifies well test analysis. World Oil,
485 196(6), 95–106.

486 Cardiff, M., Bakhos, T., Kitanidis, P. K., & Barrash, W. (2013). Aquifer heterogeneity characterization with oscillatory pumping:
487 Sensitivity analysis and imaging potential. *Water Resources Research*, 49, 5395‑5410. https://doi.org/10.1002/wrcr.20356.

488 Cardiff, M., & Barrash, W. (2015). Analytical and semi ‑ analytical tools for the design of oscillatory pumping tests. *Groundwater*, 53(6),
489 896‑907. https://doi.org/10.1111/gwat.12308.

490 Cardiff, M., Y. Zhou, W. Barrash, and P.K. Kitanidis (2019), Aquifer Imaging with Oscillatory Hydraulic Tomography: Application at
491 the Field Scale*. Groundwater. https://doi.org/10.1111/gwat.12960.

492 Chaudhry A. (2004). Oil Well Testing Handbook. Gulf Professional Publishing. **ISBN:** 9780750677066.

493 Cheng, Y., & Renner, J. (2018). Exploratory use of periodic pumping tests for hydraulic characterization of faults. *Geophysical Journal*
494 *International*, 212(1), 543‑565. https://doi.org/10.1093/gji/ggx390.

495 Copty, N. K., & Findikakis, A. N. (2004). Stochastic analysis of pumping test drawdown data in heterogeneous geologic formations
496 [Analyse stochastique des données de rabattement obtenues en pompages d'essai dans des formations géologiques hétérogènes]. *Journal*
497 *of Hydraulic Research*, 42(sup1), 59‑67. https://doi.org/10.1080/00221680409500048.

498 Despax, D., Dovis, R., Fedele, J. ‑ M., & Martin, J. ‑ P. (2004). Method and device for determining the quality of an oil well reserve.
499 U.S. Patent, 6, 801–857.

500 Fokker, P. A., Renner, J., Verga, F. (2013). Numerical modeling of periodic pumping tests in wells penetrating a heterogeneous aquifer.
501 *American Journal of Environmental Sciences*, 9(1), 1‑13. https://doi.org/10.3844/ajessp.2013.1.13.

502 Fokker, P. A., Salina Borello, E., Serazio, C., & Verga, F. (2012). Estimating reservoir heterogeneities from pulse testing. *Journal of*

26

Petroleum Science and Engineering, 86‑87, 15‑26. https://doi.org/10.1016/j.petrol.2012.03.017.

Fokker, P. A., Salina Borello, E., Verga, F., Viberti, D. (2018). Harmonic pulse testing for well performance monitoring. *Journal of Petroleum Science and Engineering*, 162, 446‑459. https://doi.org/10.1016/j.petrol.2017.12.053.

Fokker, P. A., Verga, F. (2011). Application of harmonic pulse testing to water‑oil displacement. *Journal of Petroleum Science and Engineering*, 79(3‑4), 125‑134. https://doi.org/10.1016/j.petrol.2011.09.004.

Gringarten, A. C., Bourdet, D. P., Landel, P. A., & Kniazeff, V. J. (1979). A comparison between different skin and wellbore storage typecurves for early‑time transient analysis. In SPE Annual Technical Conference and Exhibition. Las Vegas, Nevada: Society of Petroleum Engineers. SPE8205MS. https://doi.org/10.2118/8205‑MS.

Gringarten A.C., (2008) From Straight Lines to Deconvolution: The Evolution of the State of the Art in Well Test Analysis. SPE Reservoir Evaluation & Engineering - *SPE Reservoir Evaluation & Engineering*. 11(01) pp. 41-62. 10.2118/102079-PA.

Guiltinan, E., & Becker, M. W. (2015). Measuring well hydraulic connectivity in fractured bedrock using periodic slug tests. *Journal of Hydrology*, 521, 100‑107. https://doi.org/10.1016/j.jhydrol.2014.11.066.

Hollaender, F., Hammond, P. S., & Gringarten, A. C. (2002). Harmonic testing for continuous well and reservoir monitoring. In Proceedings - *SPE Annual Technical Conference and Exhibition*, (pp. 3071‑3082). San Antonio, TX: Society of Petroleum Engineers (SPE). https://doi.org/10.2118/77692 - MS.

Kuo, C. H. (1972). Determination of reservoir properties from sinusoidal and multirate flow tests in one or more wells. *Society of Petroleum Engineers Journal*, 12(06), 499‑507. https://doi.org/10.2118/3632 - PA.

Morozov, P. E. (2013). Harmonic testing of hydraulically fractured wells. *Proceeding of 17th European Symposium on Improved Oil Recovery*. St. Petersburg, Russia, 16 - 18 April 2013.

Olarewaju, J. S. and Lee J.W. (1989). "A Comprehensive Application of a Composite Reservoir Model to Pressure-Transient Analysis." *SPE Reservoir Engineering* 4(03). Society of Petroleum Engineers.DOI:10.2118/16345-pa.

Renner, J., & Messar, M. (2006). Periodic pumping tests. *Geophysical Journal International*, 167(1), 479–493. https://doi.org/10.1111/j.1365-246X.2006.02984.x.

Rochon, J., Jaffrezic, V., De La Combe, J.L.B., Azari, M., Roy, S., Dorffer, D., et al. (2008). Method and application of cyclic well testing with production logging. In Proceedings - *SPE Annual Technical Conference and Exhibition*, 4:2376‑90. Denver, CO. https://doi.org/10.2118/115820 - MS.

Rosa, A. J., & Horne, R. N. (1997). Reservoir description by well‑test analysis by use of cyclic flow‑rate variation. *SPE Formation Evaluation*, 12(04), 247‑254. https://doi.org/10.2118/22698 - PA.

27

531   Salina Borello, E., Fokker, P. A., Viberti, D., Espinoza, R., & Verga, F. (2017). Harmonic‑pulse testing for non‑Darcy‑effects

532   identification. *SPE Reservoir Evaluation and Engineering*, 20(02), 486‑501. https://doi.org/10.2118/183649‑PA.S.

533   Salina Borello, E., P.A. Fokker, D. Viberti, F. Verga, H. Hofmann, P. Meier, K.-B. Min, K. Yoon, and G. Zimmermann. (2019) "Harmonic

534   Pulse Testing for Well Monitoring: Application to a Fractured Geothermal Reservoir." *Water Resources Research*, 2019. 2018WR024029.

535   https://doi.org/10.1029/2018WR024029.

536   Sclumberger (2016) Signature Quartz Gauges. Product sheet.

537   Sun, A. Y., Lu, J., & Hovorka, S. (2015). A harmonic pulse testing method for leakage Detection in deep subsurface storage formations.

538   *Water Resources Research*, 51, 4263‑4281. https://doi.org/10.1002/2014WR016567.

539   Verga, F., Viberti, D., & Salina Borello, E. (2008). A new 3‑D numerical model to effectively simulate injection tests. In 70th European

540   Association of Geoscientists and Engineers Conference and Exhibition 2008: Leveraging Technology. Incorporating SPE EUROPEC

541   2008 (Vol. 2, pp. 946‑959). Rome: Society of petroleum engineers. https://doi.org/10.2118/113832‑MS.

542   Verga, F., Viberti, D., Salina Borello, E., & Serazio, C. (2014). An effective criterion to prevent injection test numerical simulation from

543   spurious oscillations. *Oil & Gas Science and Technology*‑ Revue d'IFP Energies Nouvelles, 69(4), 633–651. https://doi.org/10.2516/ogst/

544   2013137.

545   Verga F., Viberti D., Salina Borello E: (2011). A new insight for reliable interpretation and design of injection tests. *Journal of Petroleum*

546   *Science and Engineering* **78**(1) (2011) 166–177 Elsevier. doi 10.1016/j.petrol.2011.05.002.

547   Viberti, D. (2016). Effective detrending methodology for harmonic transient pressure response. *Geoingegneria Ambientale e Mineraria*,

548   149(3), 55‑62.

549   Viberti, D., Salina Borello, E., & Verga, F. (2018). Pressure detrending in harmonic pulse test interpretation: When, why and how.

550   *Energies*, 11(6), 1540 MDPI. https://doi.org/10.3390/en11061540.

551   Vinci, C., Steeb, H., & Renner, J. (2015). The imprint of hydro‑mechanics of fractures in periodic pumping tests. *Geophysical Journal*

552   *International*, 202(3), 1613‑1626. https://doi.org/10.1093/gji/ggv247.

553   Zhou, Y. and M. Cardiff, Oscillatory hydraulic testing as a strategy for NAPL source zone monitoring: Laboratory Experiments. *Journal*

554   *of Contaminant Hydrology*, 2017. 200: p. 24-34. https://doi.org/10.1016/j.jconhyd.2017.03.005.

555

556

28

557   **NOMENCLATURE**

558   ɸ porosity

559   μ viscosity

560   ω angular frequency (=2π/T)

561   λ mobility

562   η diffusivity

563   ζ multiplier associated to diffusivity

564   C wellbore storage

565   C_K C_I coefficients multiplying Bessel functions K and I respectively

566   c_t formation compressibility

567   c_t total compressibility

568   c_w water compressibility

569   f frequency

570   g_ω time-independent part of harmonic pressure component

571   h net pay

572   i complex unit

573   I_0, I_1 modified Bessel functions of the first kind

574   k reservoir permeability

575   k_h horizontal permeability

576   k_z vertical permeability

577   K_0, K_1 modified Bessel functions of the second kind

578   M mobility ratio

579   p pressure

29

580   p_{res} reservoir pressure

581   p_{well} well pressure

582   P_D dimensionless pressure

583   P_D' dimensionless pressure derivative

584   p_ω pressure harmonic component

585   q volumetric rate

586   q_{perfs} volumetric rate actually filtrating from the well

587   q_{well} imposed volumetric rate at reservoir conditions

588   q_ω rate harmonic component

589   r_{eq} equivalent radius of front position (numerical simulation)

590   r_l fluid front position between inner and outer zone (radial composite model)

591   r_w well radius

592   R pressure - rate ratio of harmonic components

593 |R| amplitude of R

594 |R'| amplitude of derivative of R with respect to $\ln(1/f)$

595   S skin

596   t_D dimensionless time

597   T oscillation period

598   T_f fundamental oscillation period

599   T* critical oscillation period

600   T_D dimensionless oscillation period

601   T_l temperature of the inner zone (radial composite model)

602   T_m median temperature of heated zone (numerical simulation)

30

603

APPENDIX A

604

605 In the following we incorporate skin in the well pressure expression and we derive the general system response in a radial composite

606 scenario of radius r_1.

607 The pressure in the well is different from the pressure at the well location in the reservoir, because of skin. Skin is introduced as an

608 instantaneous pressure drop due to, e.g., a mudcake or wellbore impairment as at term proportional to the flow rate:

609
$$p_{well} = p_{res}(r_w) + \frac{1}{2\pi h \lambda_1} q_{perfs} \cdot S \tag{23}$$

610 where $\lambda_i = \frac{k_i}{\mu_i}$ is the mobility and h is the reservoir thickness. The rate is taken positive for injection.

611 Rate is related to pressure gradient throw Darcy law. At the well sandface ($r=r_w$), considering eq. 3 we have:

612
$$q_{perfs} = -2\pi h \lambda_1 \left[r \frac{\partial p}{\partial r} \right]_{r=r_w} = -2\pi h \lambda_1 \left[r \frac{dg_\omega}{dr} \right]_{r=r_w} e^{i\omega t} \tag{24}$$

613 From eq. (7), applying the differential properties of Bessel functions (Abramowitz and Stegun, 1964) we obtain:

614
$$\frac{dg_\omega}{dr}(r) = -\zeta q_\omega C_K K_1(\zeta r) + \zeta q_\omega C_I I_1(\zeta r) \tag{25}$$

615 From eq. (3), eq. (7) and eq.(23-25), the response function, in the pulser well is:

616
$$R_\omega^{pulser} = \frac{p_{well}}{q_{well}} = \frac{1}{q_\omega e^{i\omega t}} \left\{ p_{res}(r_w) + \frac{1}{2\pi h \lambda_1} q_{perfs} \cdot S \right\} = \frac{g_\omega(r_w)}{q_\omega} - \frac{1}{q_\omega} S \left[r \frac{dg_\omega}{dr} \right]_{r=r_w}$$

617
$$= C_K^1 K_0(\zeta_1 r_w) + C_I^1 I_0(\zeta_1 r_w) + S \cdot \zeta_1 r_w \left[C_K^1 K_1(\zeta_1 r_w) - C_I^1 I_1(\zeta_1 r_w) \right]$$

618
$$\tag{26}$$

619 If we monitor an observation well, we directly see the reservoir pressure at that location. From eq. (3) and eq. (7) if the observation well

620 is inside (zone 1) or outside (zone 2) the area near wellbore with altered temperature, we respectively have:

621
$$R_\omega^{obs} = \frac{p_{well}}{q_{well}} = \frac{g_\omega(r_{obs})}{q_\omega} = \begin{cases} C_K^1 K_0(\zeta_1 r_{obs}) + C_I^1 I_0(\zeta_1 r_{obs}) & (r_{obs} < r_1) \\ C_K^2 K_0(\zeta_2 r_{obs}) + C_I^2 I_0(\zeta_2 r_{obs}) & (r_{obs} \geq r_1) \end{cases} \tag{27}$$

622 where parameters C_K^1, C_I^1, C_K^2, C_I^2 have to be determined through imposing boundary conditions and continuity at the interface. Details

623 follow in Appendix B.

APPENDIX B

624

625 This Appendix provides the details on the determination of the free parameters C_K^1, C_I^1, C_K^2, C_I^2 in the solution for the harmonic response

626 in a pulse test in a radial composite system with two zones (eq. 26 and eq. 27). The two zones have different mobility due to the different

627 viscosity resulting from the temperatures in the two zones. Coefficients C_K^1, C_I^1, C_K^2, C_I^2 have to be determined through imposing the

31

628   following conditions: (1) reservoir inflow from the wellbore; (2) continuity of pressure at the interface; (3) continuity of flow at the

629   interface; and (4) vanishing pressure disturbance at infinity.

630   We start with the inflow condition from the wellbore (condition 1). Because the wellbore has a nonzero volume (V_{well}) and the injected

631   fluid has a nonzero compressibility (c), part of the injected fluid is "stored" in the wellbore when the pressure is changing. The resulting

632   rate sandface is thus:

633

$$q_{perfs} = q_{well} - C \cdot \frac{dp_{well}}{dt} \tag{28}$$

634   where, $C = c \cdot V_{well}$ is the wellbore storage coefficient.

635   Substitution of eq. 3 and eq. 23 in eq. 28 yields:

636

$$q_{perfs} = q_\omega e^{i\omega t} - C \cdot \frac{d}{dt}\left(p_{res}(r_w) + \frac{1}{2\pi h \lambda_1} q_{perfs} \cdot S \right) \tag{29}$$

637   The time dependence of rate (eq. 3) and pressure (eq. 4) is fully contained in the factor $e^{i\omega t}$, therefore $\frac{d}{dt}[p(r_w, t)] = \frac{d}{dt}[g(r_w)e^{i\omega t}] =$

638     $i\omega g(r_w)e^{i\omega t} = i\omega p(r_w, t)$, and similarly $\frac{d}{dt}[q_{perfs}] = i\omega q_{perfs}$. Eq. 29 thus yields:

639

$$q_{perfs} = q_\omega e^{i\omega t} - C \cdot i\omega \cdot \left(p_{res}(r_w) + \frac{1}{2\pi h \lambda_1} q_{perfs} \cdot S \right) \tag{30}$$

640   Substitution of the Darcy expression for the rate at the sandface (eq.11) in eq. 30 gives:

641

$$-2\pi h \lambda_1 \left[r \frac{dg_\omega}{dr} \right]_{r=r_w} = q_\omega - i\omega C \cdot \left(g_\omega(r_\omega) - \left[r \frac{dg_\omega}{dr} \right]_{r=r_w} \cdot S \right) \tag{31}$$

642   Substituting eq. 7 in eq. 31 and grouping for C_K^1 and C_I^1 gives:

643

$$C_K^1 [2\pi h \zeta_1 r_w \lambda_1 K_1(\zeta_1 r_w) + i\omega C K_0(\zeta_1 r_w) + i\omega C \cdot S r_w \zeta_1 K_1(\zeta_1 r_w)]$$

644

$$+C_I^1 [-2\pi h \zeta_1 r_w \lambda_1 I_1(\zeta_1 r_w) + i\omega C I_0(\zeta_1 r_w) - i\omega C \cdot S r_w \zeta_1 I_1(\zeta_1 r_w)] = 1$$

645   (32)

646   This equation poses the first equation for the determination of the parameters in the solution (Eq. 7).

647   At the fluid front ($r = r_1$) between the inner zone, characterized by mobility λ_1, diffusion η_1, ζ_1,and coefficients C_K^1, C_I^1 , and the outer

648   zone, characterized by mobility λ_2, diffusion η_2, ζ_2,and coefficients C_K^2, C_I^2, continuity of pressure (condition 2) and flow rate (condition

649   3) must be guaranteed.

650   According to eq. 4 and 7, pressure of the ith zone writes:

651

$$\left(C_K^i K_0(\zeta_i r) + C_I^i I_0(\zeta_i r) \right) e^{i\omega t} \tag{33}$$

652   Imposing continuity of pressure (condition 2) at $r = r_1$, yields:

32

653
$$C_K^1 K_0(\zeta_1 r_1) + C_I^1 I_0(\zeta_1 r_1) = C_K^2 K_0(\zeta_2 r_1) + C_I^2 I_0(\zeta_2 r_1) \qquad (34)$$

654 According to Darcy law and eq. 25, flow rate of the ith zone writes

655
$$-2\pi r h \lambda_i \left[\frac{dg_\omega}{dr}\right] e^{i\omega t} = -2\pi h e^{i\omega t} q_\omega \, \lambda_i \, \zeta_i r \left[-C_K^i K_1(\zeta_i r) + C_I^i I_1(\zeta_i r)\right] \qquad (35)$$

656 Imposing continuity of flow rate (condition 3) at $r = r_1$, yields

657
$$-\lambda_1 \zeta_1 r_1 C_K^1 K^1(\zeta_1 r_1) + \lambda_1 \zeta_1 r_1 C_I^1 I_1(\zeta_1 r_1) = -\lambda_2 \zeta_2 r_1 C_K^2 K_1(\zeta_2 r_1) + \lambda_2 \zeta_2 r_1 C_I^2 I_1(\zeta_2 r_1) \qquad (36)$$

658 Finally, vanishing pressures in infinity (condition 4) requires $[g_\omega]_{r\to\infty} = 0$. Writing eq. (7) for the outer zone and remembering that for

659 $r \to \infty$ Bessel functions K vanishes while Bessel functions I go to infinity, condition 4 yields:

660
$$C_I^2 = 0 \qquad (37)$$

661 Substituting eq. 37 in eq. 36 and eq. 34 and putting together with eq. 33 we obtain a linear set of equations for the three remaining

662 unknowns as follows

663
$$\begin{pmatrix} i\omega C k_{001} + (2\pi h \lambda_1 + i\omega CS) k_{101} & i\omega C i_{001} - (2\pi h \lambda_1 + i\omega CS) i_{101} & 0 \\ k_{011} & i_{011} & -k_{012} \\ -\lambda_1 k_{111} & \lambda_1 i_{111} & \lambda_2 k_{112} \end{pmatrix} \begin{pmatrix} C_K^1 \\ C_I^1 \\ C_K^2 \end{pmatrix} = \begin{pmatrix} 1 \\ 0 \\ 0 \end{pmatrix} \qquad (38)$$

664 where

665
$$\begin{aligned} k_{001} &= K_0(\zeta_1 r_w) & k_{101} &= K_1(\zeta_1 r_w) \cdot \zeta_1 r_w \\ i_{001} &= I_0(\zeta_1 r_w) & i_{101} &= I_1(\zeta_1 r_w) \cdot \zeta_1 r_w \\ k_{011} &= K_0(\zeta_1 r_1) & k_{111} &= K_1(\zeta_1 r_1) \cdot \zeta_1 r_1 \\ i_{011} &= I_0(\zeta_1 r_1) & i_{111} &= I_1(\zeta_1 r_1) \cdot \zeta_1 r_1 \\ k_{012} &= K_0(\zeta_2 r_1) & k_{112} &= K_1(\zeta_2 r_1) \cdot \zeta_2 r_1 \end{aligned} \qquad (39)$$

666 The solution to this set of equations is easily obtainable by matrix inversion; the parameters C_K^1, C_I^1, C_K^2 will depend on skin S, wellbore

667 storage coefficient C, position of the temperature interface r_1, mobility (λ_1, λ_2) and diffusion coefficient (η_1, η_2) in the two zones and the

668 angular frequency (ω).

669

670

671

672

33